Time-resolved x-ray imaging of nanoscale spin-wave dynamics at multi-GHz frequencies using low-alpha synchrotron operation Ⓕ

View Online   Export Citation   CrossMark

S. Mayr,[1,2] ⓘ J. Förster,[3] ⓘ S. Finizio,[1] ⓘ K. Schultheiss,[4] ⓘ R. A. Gallardo,[5] ⓘ R. Narkovicz,[4] ⓘ G. Dieterle,[3]
A. Semisalova,[4,6] ⓘ J. Bailey,[1] ⓘ E. Kirk,[1] ⓘ A. Suszka,[1] ⓘ J. Lindner,[4] ⓘ J. Gräfe,[3] ⓘ J. Raabe,[1] ⓘ G. Schütz,[3]
M. Weigand,[7] ⓘ H. Stoll,[3,8] ⓘ and S. Wintz[3,7,a)] ⓘ

AFFILIATIONS

[1]Paul Scherrer Institut, 5232 Villigen PSI, Switzerland
[2]Laboratory for Mesoscopic Systems, Department of Materials, ETH Zurich, 8093 Zurich, Switzerland
[3]Max-Planck-Institut für Intelligente Systeme, 70569 Stuttgart, Germany
[4]Helmholtz-Zentrum Dresden-Rossendorf, Institut für Ionenstrahlphysik und Materialforschung, 01328 Dresden, Germany
[5]Universidad Técnica Federico Santa María, Valparaíso, Chile
[6]Universität Duisburg-Essen, 47057 Duisburg, Germany
[7]Helmholtz-Zentrum für Materialien und Energie, 14109 Berlin, Germany
[8]Johannes Gutenberg-Universität Mainz, Institut für Physik, 55128 Mainz, Germany

[a)]Author to whom correspondence should be addressed: sebastian.wintz@helmholtz-berlin.de

ABSTRACT

Time-resolved x-ray microscopy is used in a low-alpha synchrotron operation mode to image spin dynamics at an unprecedented combination of temporal and spatial resolution. Thereby, nanoscale spin waves with wavelengths down to 70 nm and frequencies up to 30 GHz are directly observed in ferromagnetic thin film microelements with spin vortex ground states. In an antiparallel ferromagnetic bilayer system, we detect the propagation of both optic and acoustic modes, the latter exhibiting even a strong non-reciprocity. In single-layer systems, quasi-uniform spin waves are observed together with modes of higher order (up to the 4th order), bearing precessional nodes over the thickness of the film. Furthermore, the effects of magnetic material properties, film thickness, and magnetic fields on the spin-wave spectrum are determined experimentally. Our experimental results are consistent with numerical calculations from a micromagnetic theory even on these so-far unexplored time- and length scales.

I. INTRODUCTION

Spin waves are the collective precessional excitations of ordered spin systems with their excitation quantum being referred to as magnon.[1,2] In the associated research field of magnonics, spin waves are envisioned for logic and signal processing applications.[3,4] The potential advantage of employing spin waves instead of present charge-based microelectronic technology stems from both the absence of Ohmic losses in the spin-wave signal transfer (power consumption) and a better miniaturization prospect given by their much shorter wavelengths as compared to electromagnetic waves of the same frequency.[5,6] A further promising aspect of spin waves is their intrinsically non-linear

dynamics[7] that could be exploited for unconventional information processing schemes,[8] such as neuromorphic computing.[9–11] Moreover, quantum magnonics[12] yields an interesting perspective for quantum technologies, considering room-temperature magnon Bose–Einstein condensates,[13] magnon–photon coupling,[14] and magnon entanglement.[15,16] For the majority of implementation scenarios for magnonic devices, it will be highly beneficial to utilize spin waves of nanoscale wavelengths, namely, because of areal footprint and signal propagation speed following from the typically higher group velocities of shorter waves.[4] At the same time, there is a strong demand for high operation frequencies as these directly scale with the processing bandwidth.[6]

27 February 2025 10:12:26

In general, spin waves occur at frequencies (f) up to the THz regime and with wavelengths (λ) down to the atomic scale.[4] The system-specific correspondence between frequency and wavenumber $k = 2\pi/\lambda$ is referred to as the spin-wave dispersion relation $f(k)$. This relation depends on the micromagnetic energy terms in the system, for which the most prominent (among other potential contributions) are the magnetodipolar energy (dominant for long wavelengths), exchange energy (dominant for short wavelengths), anisotropy energy, Zeeman energy,[17] and Dzyaloshinskii–Moriya energy[18,19] where it applies. A useful quantity to determine the respective influence of dipolar and exchange effects in the dispersion relation with respect to λ is the exchange length $L_{ex} = \sqrt{2A/\mu_0 M_s^2}$, with A being the exchange constant, μ_0 being the vacuum permeability, and M_s being the saturation magnetization. For waves with wavelengths much larger than the exchange length, the long-range dipolar interaction dominates. However, if the wavelength approaches values that are an order of magnitude larger than, or even comparable to L_{ex}, the exchange interaction becomes more relevant and eventually the dominating factor. In thin film systems, which prospectively are most relevant for applications, the spin-wave dispersion relation is anisotropic for the magnetization ($\mathbf{M}$) being in plane,[17] concerning the relative orientation of wavevector ($\mathbf{k}$) and $\mathbf{M}$, with $\mathbf{M} \parallel \mathbf{k}$ being referred to as backward-volume waves and $\mathbf{M} \perp \mathbf{k}$ referred to as Damon–Eshbach waves.[20] On the contrary, when $\mathbf{M}$ is oriented normal to the film plane, the lateral dispersion relation remains isotropic (forward volume waves).[17]

Soft magnetic materials typically have spin-wave frequencies of the order of 1–10 GHz for the uniform ferromagnetic resonance ($\lambda \to \infty$) down to wavelengths of the order of 100 nm.[21] Significantly higher frequencies can be achieved in materials with high magnetic anisotropies or in ferrimagnetic/antiferromagnetic systems.[6] However, such systems are often not trivial to fabricate reliably by standard means or are difficult to probe in the case of small or zero net magnetization. Alternatively, a way to go beyond the mostly considered fundamental spin-wave spectra of soft ferromagnetic thin films is by introducing discrete precessional nodes along their thickness profile.[22,23] In single-layer films, this typically leads to an increase in frequencies compared to the fundamental mode. For films above a specific thickness to exchange length ratio, however, the opposite effect may occur, namely, that the frequencies of nodal modes are lower than those of the fundamental one below a specific wavelength.[21,24,25] Similar effects were also found in magnetic heterostructures, such as antiparallel magnetic bilayers separated by a thin non-magnetic interlayer.[26,27] Here, acoustic modes lead to lower precession frequencies, while optic modes are shifted to higher frequencies.[26,28–30]

Apart from finding a suitable spin-wave dispersion relation, the coherent excitation of nanoscale spin waves imposes a critical challenge. Antennas based on metallic conductors have proven useful for the excitation of spin waves with wavelengths above the minimum feature size of the antenna.[31] In this case, an alternating electric current flowing in the conductor generates a spatially inhomogeneous Oersted field that causes the excitation of spin waves. However, it becomes increasingly difficult to fabricate such antennas with feature sizes on the scale of 100 nm and below, while keeping a sufficient impedance matching of the electric circuit. Other short-wavelength excitation methods rely on parametric pumping[13,17,32] or spin-transfer/orbit torque effects.[33,34] What has proven very useful recently in this context is the coupling of a uniform magnetic field excitation to the internal field

landscape of inhomogeneous systems[35–38] or, in particular, naturally stabilized non-collinear spin textures, such as domain walls,[28,39–42] vortices,[24,27,28,43–46] or skyrmions.[47]

For achieving a fundamental understanding of spin-wave dynamics at nanoscale wavelengths and high frequencies, magnetic imaging techniques combining very high spatial and temporal resolution are of critical importance. While electron or scanning probe microscopies typically offer very high spatial magnetic resolution, they are often quite limited in time resolution, apart from a few promising exceptions.[48–51] On the other hand, optical magnetic microscopy typically offers excellent time resolution but is limited spatially to the diffraction limit of visible light, except when operating in the near field.[52,53] In addition to imaging, there are also magnon spectroscopy techniques, detecting the existence as well as the energy or frequency vs momentum transfer or wavenumber dependence of magnons. Among these techniques are neutron scattering,[54] resonant inelastic x-ray scattering[55] and spin-polarized electron energy loss spectroscopy[56,57] for magnons with wavelengths on the atomic scale. Complementarily, for magnons above the visible light limit, Brillouin light scattering has proven a viable tool,[58,59] which can even be equipped with high spatial resolution[60,61] though at a reduced wavenumber sensitivity. Note that while imaging techniques are essentially only sensitive to coherent magnons on a discrete grid of frequencies, spectroscopy techniques are sensitive to both coherent and incoherent magnons of continuous frequency. As an intermediate method, all electrical spin-wave spectroscopy[37,38,62,63] is sensitive to coherent magnon transport down to wavelengths of the order of ~10 nm, indirectly, by measuring frequency and correlated phases between emitting and detecting antennas.

Against this background, soft x-ray magnetic microscopy at synchrotron facilities allows for a unique combination of spatial and stroboscopic temporal resolution of the order of 10 nm and 100 ps.[64–67] When furthermore exploiting the special low-alpha operation mode of the synchrotron (a mode with shorter x-ray flashes),[24,68,69] the time resolution can be improved to an order of 10 ps as demonstrated in this work.

Here, we demonstrate that scanning transmission x-ray microscopy (STXM) can be used to image various short-wavelength spin-wave modes with wavelengths down to 70 nm at frequencies up to 30 GHz by utilizing the low-alpha operation mode at the Bessy II synchrotron.

In the first part, non-reciprocal spin waves of both acoustic and optical modes are observed for a ferromagnetic bilayer system, where the two ferromagnetic layers are aligned antiparallel to each other. In the second part, single ferromagnetic layer systems are investigated upon variation of magnetic material parameters, layer thicknesses, and through the application of an external magnetic bias field. Here, spin waves of the fundamental quasi-uniform mode in the Damon–Eshbach geometry are imaged as well as higher-order modes—which possess precessional nodes along the thickness of the film—up to the fourth order. The results are corroborated and complemented by numeric results from the dynamic matrix method, which is an analytic micromagnetic model based on coupled Landau–Lifshitz (LL) equations, suitable for continuous ferromagnetic films.

II. EXPERIMENT

The samples were directly imaged using time-resolved (TR)-STXM,[70–74] which was carried out at the MAXYMUS[67] end station of

27 February 2025 10:12:26

the BESSY II synchrotron radiation facility of Helmholtz-Zentrum Berlin. In TR-STXM measurements, monochromatic soft x rays are focused onto the sample by a Fresnel zone plate (diffractive lens) to a spot of $\sim$25 nm in diameter and the photons transmitted through the sample are detected by a point detector. To form a two-dimensional image, the sample is raster scanned through the beam. The energy of the photons was tuned either to the Fe ($\sim$709 eV) or Co ($\sim$781 eV) L_3 resonant x-ray absorption edges for sensitivity to the NiFe, Co, or CoFeB layers in our samples. We utilized circularly polarized X rays to gain magnetic contrast via the x-ray magnetic circular dichroism (XMCD) effect.[75]

To perform time-resolved measurements, we employed a pump-probe technique, where the excitation of the sample is synchronized to the probing x-ray flashes from the synchrotron. Each photon detection event by the avalanche photodiode (APD) is routed to a specific counter of a register set by a field-programmable gate array (FPGA) in real time. By using an APD with a bandwidth higher than the repetition rate of the synchrotron ($\sim$500 MHz), it is possible to resolve two consecutive x-ray flashes, where the time resolution is defined by the width of the electron bunches generating the x-ray flashes. For the experiments presented here, we utilized the low-alpha optics multibunch mode offered by BESSY II to reach a time resolution of the order of 10 ps, which allowed us to image dynamics exceeding 30 GHz.

For the synchronization between the pump and the probe signals, the applied frequencies have to be commensurate with the time structure of the synchrotron. For an RF signal, this means that they have to fulfill the relation

$$f = 500 \text{ MHz} \times \frac{M}{N},$$

where N is the number of channels and M is an integer chosen to match the desired frequency with N and M coprime. The number of channels N determines into how many counters the photons are routed and equals the number of frames of the time-resolved movie. For a better visibility of the dynamics, the images are typically normalized, which means that each frame of the movie is divided by the average of all frames. Subsequently, a Gaussian filter is applied that slightly blurs the normalized images, which improves the visibility of the spin-wave dynamics.

III. RESULTS

A. Spin waves in magnetic bilayer vortex pairs

The first sample system investigated was a trilayer, consisting of two ferromagnetic layers [$Ni_{81}Fe_{19}$ (NiFe) and Co] each of 50 nm thickness, separated by a 10-nm-thick Cu interlayer [see Fig. 1(a), all thicknesses are nominal]. Out of this stack, micrometer-sized elements were patterned as detailed in the Appendix. In the following, we discuss the example of spin-wave dynamics observed in a disk element of 2 μm diameter.

Following subsequent demagnetization cycles applied, this sample was found to exhibit two different sets of remanent states, namely, that of stacked vortex pairs with either opposite or equal vortex circulations (one vortex in each layer) [see Figs. 1(b), 1(c), 2(a), and 2(b) and Ref. 76]. Such a bistable behavior can be expected for laterally confined dipolar-coupled layers, for which the Cu thickness is above the range for which interlayer exchange coupling is mediated. Nevertheless, there could possibly be a roughness-induced interlayer coupling present in the system, with typically an energetic preference for parallel alignment of the layers.[77]

1. Antiparallel vortex circulations

For the case of opposite vortex circulations at remanence, we imaged the M_x-component and thereby the vortex in-plane states of NiFe [Fig. 1(b)] and Co [Fig. 1(c)] separately by STXM using a single x-ray helicity. While opposite vortex circulations can clearly be identified [$C_{Co} = +1$ and $C_{NiFe} = -1$], it was found that the vortex core positions were not always identical in both layers, i.e., the cores may exhibit a relative lateral shift to each other, while the core polarizations were not directly resolved. Such core shifts occurred varying in
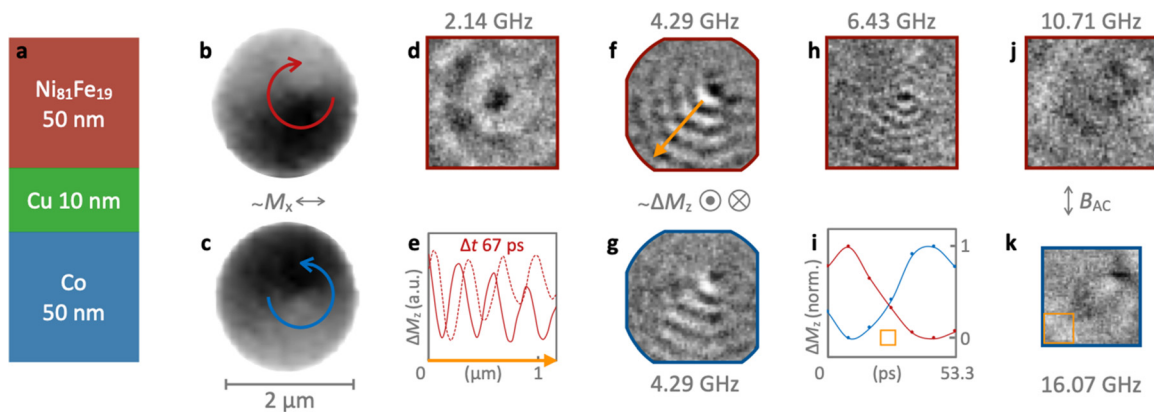
FIG. 1. Spin-wave dynamics in a Co/Cu/NiFe disk element being in a vortex pair state with antiparallel circulations. (a) Schematic of the stack with nominal layer thicknesses. (b) and (c) STXM images of (b) NiFe and (c) Co with in-plane sensitivity, arrows indicating the vortex circulations. All STXM images are to scale (scale bar below (c)). Images in the upper row correspond to the NiFe layer (red) and images in the bottom correspond to the Co layer (blue). (d), (f), (g), (h), (j), and (k) Normalized TR-STXM snapshots of spin waves in the (d), (f), (h), and (j) NiFe and (g) and (k) Co layer driven by alternating field excitations of the denoted frequencies, highlighting temporal magnetic changes ($\sim\Delta M_z$). (e) Interpolated line profiles along the orange arrow in (f) for a relative time delay of 67 ps confirming wave propagation. (i) Normalized areal magnetic contrast ($\sim\Delta M_z$) over time of the orange boxed region in (k), separately for the NiFe layer (red dots) and the Co layer (blue dots) with corresponding interpolated lines. In our reference frame, z is normal to the stack, while x and y lie in the plane of the film.

27 February 2025 10:12:26
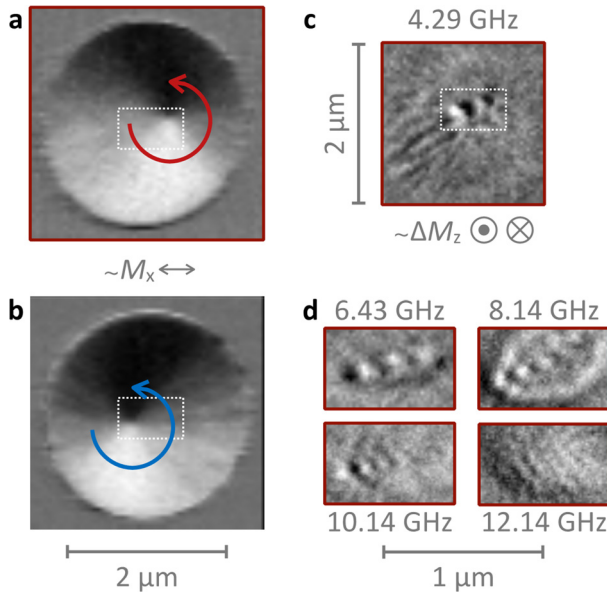
FIG. 2. Spin-wave dynamics in the Co/Cu/NiFe disk element being in a vortex pair state with parallel circulations and displaced cores. (a) and (b) STXM images of Co and NiFe with in-plane sensitivity using both x-ray helicities, arrows indicating the vortex circulations. (c) TR-STXM snapshot of spin waves in NiFe at 4.29 GHz propagating between the two cores: normalized image with dynamic perpendicular magnetic sensitivity ($\sim\Delta M_z$). (d) Normalized TR-STXM snapshots (ΔM_z) of the NiFe layer for different excitation frequencies as indicated.

magnitude for both static and magnetically excited cases. Possible reasons for these shifts could lie in a potential thickness gradient in one or both of the magnetic layers, a repulsive coupling between antiparallel vortex core polarizations,[78] or the dynamic excitation of the cores.

When the disk element with opposite vortex circulation state is excited by an alternating quasi-uniform magnetic field of 4.29 GHz frequency and $\sim$1 mT in magnitude, spin waves with sub-micrometer wavelengths are excited at the vortex cores in both layers and subsequently propagate to the rim of the disk, as imaged by TR-STXM [see Figs. 1(f) and 1(g) and movie M1 of the supplementary material (SM)]. These waves can be seen in the normalized snapshots highlighting the temporal magnetic changes in the sample ($\sim\Delta M_z$), separately for NiFe [Fig. 1(f)] and Co [Fig. 1(g)]. By comparing the spin-wave response of the two different layers, it becomes obvious that they locally exhibit the same phase in their dynamic M_z component. In that way, the waves observed correspond to the layer-collective acoustic mode of antiparallel ferromagnetic bilayers in the Damon–Eshbach geometry ($\mathbf{M_{eq}} \perp \mathbf{k}$),[26] with the latter being always geometrically fulfilled for radial waves in a vortex state. This kind of mode was found earlier to be strongly non-reciprocal in the sense that waves of the same frequency propagating into opposite directions exhibit substantially different wavelengths.[26,27,79,80] That is also the reason why, for the outward propagating waves in the present case, reflections at the sample boundary are not apparently visible.[27,28,45]

The excitation mechanism behind the spin waves observed is based on the driven lateral oscillation of the nanoscopic magnetic vortex cores, similar to the action of a stirrer in a fluid medium.[24,27,28,43–46] The alternating magnetic field couples to the entire magnetic

structure, causing the vortex cores to be displaced, resulting in very high local magnetic torques as the source for the spin-wave generation.[24] In contrast to earlier findings, however, the spin-wave emission in the present experiment is notably asymmetric: Waves are mainly emitted toward the lateral bottom half of the disk ($-y$), while almost no waves are present in its upper half ($+y$). Assuming that one of the cores was more dynamically susceptible, this asymmetry could be a consequence of the relative lateral displacement of the vortex cores, causing a local region to be in the parallel magnetic state, which, in turn, leads to a mismatch in the dispersion relation potentially acting as a magnon block. The outward propagating nature of the visible spin-wave segment is highlighted by means of line profiles for a relative delay time of 67 ps [Fig. 1(e)] along the orange arrow in Fig. 1(f).

So far, vortex-based spin-wave emission in antiparallel magnetic bilayers was observed mainly for frequencies below 5 GHz using TR-STXM.[27,28,43,45,80] Exploiting the improved time resolution of the low-alpha operation mode of BESSYII, we were able to extend this range by more than a factor of three as will be shown in the following. Figures 1(d), 1(f), and 1(h) show the spin-wave response of the disk for frequencies between 2.14 and 6.43 GHz as normalized TR-STXM snapshots ($\sim\Delta M_z$) of the NiFe layer (see also SM movie M2). As shown above, the behavior of the Co layer is qualitatively the same for ΔM_z. For all these frequencies, spin waves are efficiently generated at the vortex cores and the resulting wavelength can be continuously tuned by the driving frequency, in agreement with earlier findings.[27] Here, the wavelengths decrease from (600 ± 80) nm at 2.07 GHz, via (320 ± 27) nm at 4.29 GHz, to (200 ± 20) nm at 6.43 GHz. At frequencies above that, the excitation efficiency is found to decrease (possibly due to the finite size and decreasing susceptibility of the vortex core pair). Nevertheless, waves of short wavelengths could be detected in the dynamic data for frequencies up to 9.64 GHz [$\lambda = (114 \pm 10)$ nm].

At a frequency of 10.71 GHz, longer waves [$\lambda = (454 \pm 114)$ nm] with opposite phase propagation direction (inward) appear in the dynamic response [Fig. 1(j), Suppl. Fig. S1, and SM movie M2]. Given the strong non-reciprocity of the system, this situation suggests that the outward propagating waves belong to the short-wavelength branch of the collective acoustic mode of the antiparallel bilayer, while the inward propagating waves are part of the long-wavelength branch which would also fit to the relative equilibrium circulation configuration ($C_{Co} = +1$, $C_{NiFe} = -1$).[27] Finally, for a frequency of 16.07 GHz, we observed inward propagating waves with even longer wavelength estimates (932 ± 233) nm, as shown in Fig. 1(k) and Suppl. Fig. S1. These waves are presumably an instance of the collective optical mode of the antiparallel bilayer[26] as it will be discussed in more detail at a later point.

It should be noted that while we provide some possible explanations for the relative lateral core shifts and the spin-wave emission asymmetry, it is not a specific focus of this work, and the origins of these effects were not unambiguously resolved.

2. Parallel vortex circulations with shifted cores

For the case of parallel vortex circulations in the ferromagnetic layers of the disk, the two vortex cores always exhibited a more pronounced relative lateral shift of the order of 500 nm to each other. This can be seen, for example, by means of static magnetic STXM images with in-plane magnetic sensitivity, exploiting both x-ray helicities [see

Figs. 2(a) and 2(b)] separately for Co and NiFe. Here, both vortices are clearly in the C = +1 state with off-centered and oppositely shifted cores, leaving the area between them to be aligned antiparallel in contrast to the other parts of the sample. The possible reasons for this relative core shift are the same as for the case of antiparallel circulations, where the shift magnitude can be easily higher for parallel circulations as the energetic effect of oppositely shifted cores is almost self-compensating from a magneto-dipolar point of view.
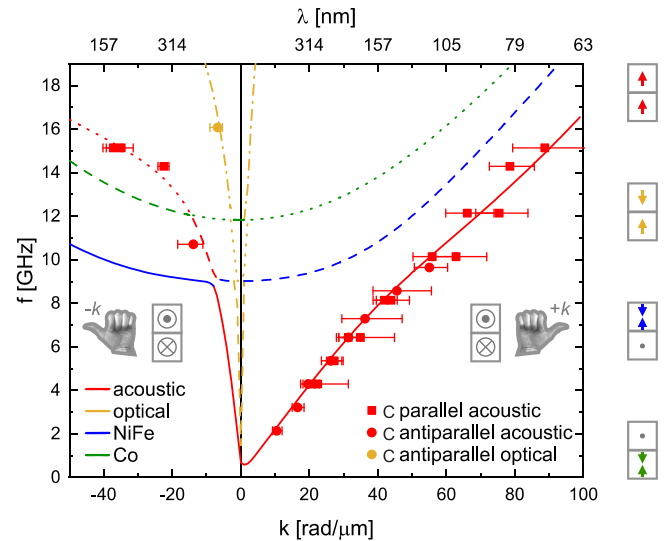
When the sample in this parallel vortex circulation state is excited by alternating magnetic fields, we observe the same kind of acoustic collective spin-wave mode as before to propagate within the region between the laterally shifted vortex cores, where the magnetic orientation of the two ferromagnetic layers is antiparallel. Figure 2(c) shows a TR-STXM snapshot with perpendicular normalized absorption contrast (right, $\sim\Delta M_z$) for the NiFe layer to an excitation of 4.29 GHz (see also SM movie M3). Within the region between the cores, waves are traveling from the position of the Co core to that of the NiFe core at a wavelength of (290 ± 80) nm. In the same way, waves can be excited continuously toward higher frequencies, as shown in the normalized TR-STXM snapshots for the NiFe layer in Fig. 2(d) for 6.43 GHz [(190 ± 40) nm], 8.14 GHz [(148 ± 16) nm], 10.14 GHz [(107 ± 13) nm], and 12.14 GHz [(89 ± 9) nm]. Note that, again, the waves in the Co layer are in phase with the NiFe layer with respect to M_z. From the given experimental data points and as expected, we can already conclude that as long as the magnetic bilayers locally couple antiferromagnetically, the spin-wave dispersion of the short-wavelength branch of the acoustic mode is the same, independent from the surrounding magnetic configuration, in particular, the overall vortex circulation states of the disk element. Furthermore, at excitation frequencies of 14.29 and 15.14 GHz, we observed simultaneously non-reciprocal waves with opposing phase propagation directions, presumably belonging to the short-wavelength branch [(80 ± 7) nm and (71 ± 8) nm, Co to NiFe core propagation] and the long-wavelength branch [(280 ± 20) nm and (175 ± 17) nm, NiFe to Co core propagation] of the acoustic mode.

3. Spin-wave dispersion in the antiparallel magnetic bilayer

To gain further insight into the relevant spin-wave dispersion relations $f(k)$ of the present antiparallel magnetic bilayer system in the Damon–Eshbach geometry, the experimental data points were plotted as solid dots (antiparallel vortex circulations) and solid squares (parallel vortex circulations) in Fig. 3. As schematically shown, positive k-values correspond to the right-handed chirality of $M_{Co,NiFe}$ and k, while the left-handed chirality corresponds to negative k.

On the $+k$ side, all data points ($\sim$2–15 GHz, $\sim$10–90 rad/μm) lie mainly on a line with a positive slope, originating approximately at zero. This situation corresponds to a linear spin-wave dispersion, where the phase velocity $v_f = 2\pi f/k$ is equal to the group velocity $v_g = 2\pi (df/dk)$, meaning that waves of all different wavelengths travel with the same speed. This part of the plot furthermore substantiates that the overall relative vortex circulation configuration (antiparallel or parallel) does not significantly influence the spin-wave dispersion relation as long as the relative layer orientation is locally antiparallel (dots and squares follow the same line).

At the negative k-branch, the data points span a smaller frequency range between $\sim$10 and $\sim$16 GHz at k-values between $\sim$5 and

FIG. 3. Spin-wave dispersions $f(k)$ of the Damon–Eshbach geometry in the Co/Cu/NiFe sample with antiparallel ferromagnetic layers. Experimental data points from TR-STXM of the disk element are shown as dots (antiparallel vortex circulations) and squares (parallel circulations, spin waves measured in the antiparallel region between the cores). Red data points correspond to the M_z-acoustic collective mode, while the yellow point is part of the M_z-optical mode. Calculated spin-wave dispersion relations are shown as lines where colors refer to the characteristic spin-wave modes: M_z-acoustic (#1, red), M_z-optical (#2, yellow), NiFe (#3, blue), Co (#4, green) and types denote the continuous spin-wave bands: (#i, solid) (#ii, dashed) (#iii, dotted), and (#iv, dashed-dotted). Hands indicate the chirality of k with respect to the magnetic equilibrium orientation of the two layers. Schematics on the right show the general dynamic mode profiles and symmetries.

$\sim$40 rad/μm, meaning that for the same frequency, the wavelengths along $+k$ are shorter than along $-k$ (short-wavelength vs long-wavelength branch). This kind of dispersion non-reciprocity is in line with earlier findings[79] for the M_z-acoustic layer-collective Damon–Eshbach modes of antiparallel bilayers, yet here less pronounced than for cases of thinner non-ferromagnetic interlayers.[27] While the red-colored $-k$ data points below 16 GHz exhibit a monotonous increase in f over k, the one at $\sim$16 GHz (yellow) falls out of this sequence. It will be shown that this point corresponds to the higher-energy M_z-optical mode of the system.

To substantiate the above interpretations, we applied an analytic micromagnetic model based on the dynamic matrix approach to calculate the spin-wave dispersion relations of the system, considering plane spin waves in infinite layers and a sublayer discretization while omitting electromagnetic effects and retardation (see the Appendix).[28,81] The problem is then solved numerically, allowing for a reasonable variation of nominal magnetic/material property parameters (see the Appendix) for an improved matching with the experimental data points (manual fit). Note that such calculations can only be considered to model the experimental spin-wave dispersion relations accurately down to wavelengths that correspond to the finite structure sizes investigated.

The four lowest-energy dispersion relations resulting from these calculations are shown as lines in Fig. 3 together with the experimental data points. The color/type line coding is as follows: Colors (red, yellow, blue, green) correspond to specific spin-wave *modes*, which refers

to the distinct character or precession profile of magnetization dynamics, e.g., m_z-acoustic (red) or m_z-optical (yellow). These modes, however, are not necessarily continuous in the dispersion plane, but they may hop between continuous spin-wave *bands* (indicated by line type: solid, dashed, dotted, dashed-dotted) at their avoided crossing points.

From these results, it can be seen that the experimental data points match the short-wavelength branch of the collective M_z-acoustic mode (red lines) in the $+k$ range and also for the long-wavelength branch in the $-k$ range there is a reasonably good agreement. Moreover, and as mentioned above, the experimental data point at around 16 GHz matches the calculated dispersion of the M_z-optical mode, from which it can be concluded that this mode—in some way an analog of antiferromagnetic resonances—was, in fact, directly observed [Fig. 1(i)].

In addition to the experimental results, one can deduce the following from the calculated results: The M_z-acoustic mode is rather linear on the $+k$ side, but exhibits a slight bend at medium k-values. It further forms a finite spin-wave gap of $\sim$500 MHz, below which propagating spin waves do not exist. This minimum is not located at $k = 0$ but shifted to positive $k \approx 2$ rad/μm, meaning that there is a small k range with opposing phase and group velocities. For negative k-values, the dispersion is also linear for frequencies up to $\sim$10 GHz with a higher slope than in the $+k$ range (non-reciprocity). At higher frequencies, however, the $-k$ dispersion curve continuously flattens to smaller slopes. In contrast to the short-wavelength branch of the M_z-acoustic mode, its long-wavelength branch intersects with two additional modes at $\sim$9 GHz (mode #3, blue) and at $\sim$12 GHz (mode #4, green).

The M_z-optical mode has a spin-wave gap of $\sim$1.5 GHz, which appears to be close to $k = 0$. It exhibits rather linear yet slightly concave dispersion branches on either k side. These branches of very high slope are also non-reciprocal, however, with an inverted sense and less pronounced than in the M_z-acoustic case. Intersections with modes #3 and #4 occur in both k directions of the M_z-optical mode.

While there are no experimental data points for modes #3 and #4, our calculations indicate that they can be characterized rather as first higher-order precessions (see also Sec. III B) of the individual magnetic layers NiFe [mode #3 (blue)] and Co [mode #4 (green)], respectively. They appear at higher frequencies (NiFe: $\sim$9 GHz) (Co: $\sim$12 GHz) and exhibit parabolic-like precession branches that are almost symmetric in k.

B. Spin waves in magnetic single-layer disks

The second sample system consists of patterned disks of single ferromagnetic layers [NiFe and $Co_{40}Fe_{40}B_{20}$ (CoFeB)] of various thicknesses. The fabrication for these samples is described in detail in the Appendix. The ground state of each sample is a magnetic vortex. Unlike the previously described trilayers, single layers typically do not exhibit any spin-wave non-reciprocity in k, and therefore, it is sufficient to focus on positive wavevectors.

1. Multimode spin-wave dynamics

Different spin-wave modes were measured by TR-STXM for a particular material and thickness combination, as exemplarily shown for a 100-nm-thick CoFeB sample (CoFeB100) (disk of 2 μm diameter), together with their theoretical dispersion curves in Fig. 4. The
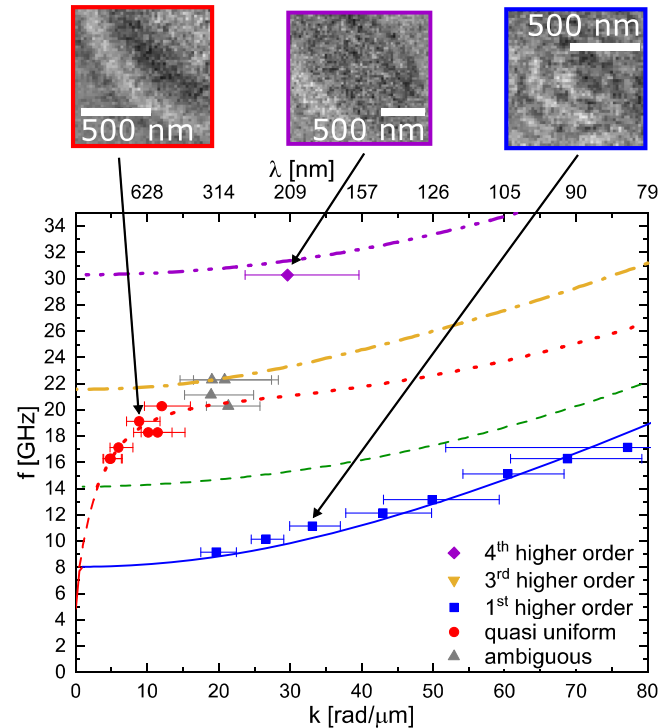
FIG. 4. Measured and calculated spin-wave dispersion relations in the Damon–Eshbach geometry in a 100-nm-thick CoFeB sample. Symbols correspond to experimentally measured data and lines to calculated dispersion curves. The colors denote the spin-wave mode, and the line styles denote the spin-wave band. The error bars represent the uncertainty in determining the wavelength. At the top, normalized STXM images are shown of the selected data points indicated by the colored arrows for different modes.

theoretical curves were calculated with the same model as previously described for the trilayers (see the Appendix). The parameters found from the manual fit are shown in the Appendix. The experimental results show that, with TR-STXM, the first higher-order spin-wave mode of the Damon–Eshbach geometry, which exhibits an inhomogeneous precession profile comprising a node over the film thickness,[21,24,25] was measured in a frequency range from 9.1 to 17.1 GHz with wavevectors of 19.7–77.2 rad/μm. This corresponds to wavelengths down to 81 $\pm$ 40 nm. Furthermore, information on the details higher-order precession profiles can be found in Ref. 24. For frequencies from 16.3 to 20.3 GHz with wavevectors of 5.0 to 21.4 rad/μm, spin waves of the standard quasi-uniform mode were imaged. Above k-values of $\sim$3 rad/μm, the first- and second-order modes occur at frequencies below the quasi-uniform mode leading to points of avoided crossings at $\sim$8 GHz and $k = 1$ rad/μm as well as 14 GHz and $k = 3$ rad/μm, respectively. However, note that these avoided crossing points are calculated for the infinite thin film limit at wavelengths above the size of the disk investigated. At 22.3 GHz, spin waves with wavevectors of 19.1 and 20.8 rad/μm were observed, which correspond either to the quasi-uniform or the third higher-order mode. Spin waves at 30.3 GHz were observed with a wavevector of 29.6 rad/μm, corresponding to a wavelength of 212 $\pm$ 53 nm, which fits with the calculated dispersion of the fourth higher-order mode. Exemplary

27 February 2025 10:12:26
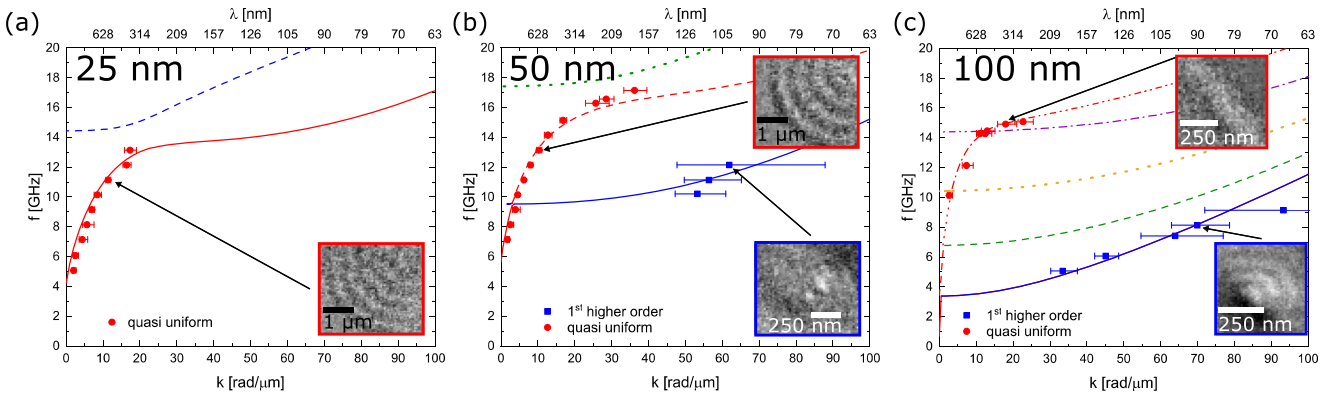
FIG. 5. Influence of the film thickness on measured and calculated dispersion relations for spin waves in the Damon–Eshbach geometry in NiFe samples. The nominal thicknesses are (**a**) 25 nm, (**b**) 50 nm, and (**c**) 100 nm. Symbols correspond to experimentally measured data, lines to calculated dispersion curves. The colors denote the spin-wave mode, and the line styles denote the spin-wave band. The error bars represent the uncertainty of the wavelength. The insets show normalized TR-STXM snapshots of selected data points for different modes, as indicated by the arrows.

normalized STXM snapshots of three different modes are shown in the top part of the figure, with the arrows indicating the corresponding data point (see also SM movie M4).

2. Influence of the film thickness

The influence of the film thickness on the spin-wave modes is shown in Fig. 5 for NiFe films with a nominal thickness of 25 nm (NiFe25), 50 nm (NiFe50), and 100 nm (NiFe100) where all disk diameters are 5 μm (see also SM movie M5). In Fig. 5(a), the spin-wave dispersions in the Damon–Eshbach geometry are shown for the 25-nm-thick film. In the considered frequency range from 0 to 20 GHz, only the quasi-uniform and first higher-order mode exist. In the STXM experiments, only spin waves belonging to the standard quasi-uniform mode were observed for frequencies from $\sim$6 to 13 GHz with wavevectors from 6 to 17.5 rad/μm.

For a doubled film thickness of 50 nm [Fig. 5(b)], the higher-order modes shift toward lower frequencies, partially below the quasi-uniform mode, which leads to an avoided crossing between the quasi-uniform and first higher-order mode at $\sim$9.5 GHz and $k = 3.5$ rad/μm [Fig. 6(b)]. Experimentally, spin waves corresponding to both modes were observed. For the quasi-uniform Damon–Eshbach mode, they are located at wavevectors of 1.7 and 36.2 rad/μm for frequencies ranging from 7.1 to 17.1 GHz. The spin waves belonging to the first higher-order mode occurred at frequencies of 10.1–12.1 GHz with wavevectors of 53.2–61.9 rad/μm. This latter wave vector corresponds to a wavelength down of 102 $\pm$ 30 nm.

When the film thickness is doubled again to 100 nm, modes of even higher order appear in the considered frequency range in the calculations, as all modes shift toward lower frequencies [Fig. 5(c)]. This leads to more points of avoided crossing between the quasi-uniform mode and the modes of higher order. These are located at $\sim$3.4 GHz and $k = 0.5$ rad/μm for the first, at 6.8 GHz and $k = 1.0$ rad/μm for the second, at 10.4 GHz and $k = 3.5$ rad/μm for the third, and at 14.6 GHz and $k = 13.0$ rad/μm for the fourth higher-order mode. In the vicinity of these avoided crossing points, for wavevectors below 15 rad/μm and frequencies between 10 and 15 GHz, some experimental data points

cannot unambiguously be attributed to the quasi-uniform or the third/ fourth higher-order mode. However, in the short-wavelength regime, the waves belonging to the first higher-order mode can be clearly identified in a frequency range of 5.1–9.1 GHz with wavevectors of 33.5–93.4 rad/μm. This means that spin waves with wavelengths down to 67 $\pm$ 20 nm were measured. A comparison between Figs. 4 and 5(c) additionally illustrates the influence of different materials on the dispersion relations. For CoFeB, which has a higher saturation magnetization and, more importantly, a higher exchange interaction than NiFe, higher-order spin-wave modes appear at higher frequencies in the TR-STXM measurements, as supported by the calculations.
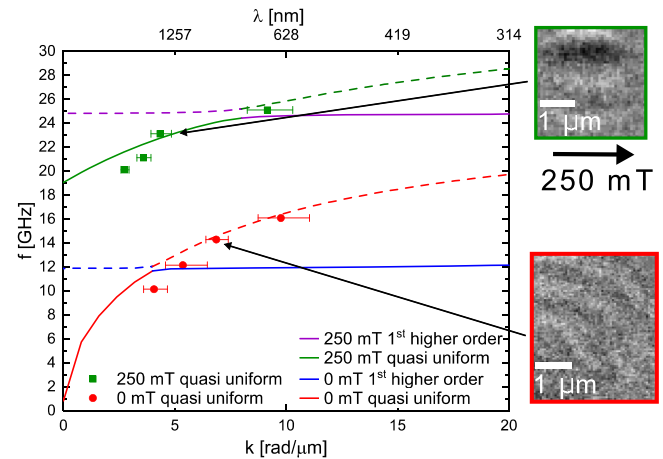
FIG. 6. Influence of a static magnetic bias field on the measured and calculated dispersion relations in the Damon–Eshbach geometry in a 50-nm-thick CoFeB sample. Symbols correspond to TR-STXM data, lines to calculated dispersion curves of the quasi-uniform and first higher-order mode. The colors denote the spin-wave mode, and the line styles denote the spin-wave band. The error bars indicate the uncertainty in determining the wavelength. On the right-hand side, normalized snapshots of TR-STXM measurements are depicted with and without the magnetic bias field applied as indicated by the arrows.

3. Influence of magnetic fields

One possibility to alter and control the dispersion relation for a given material and thickness is by applying a static magnetic bias field to the sample. Applying a field of 250 mT in the film plane expels the vortex from the disk and leads to a single-domain state with a quasi-uniform magnetic orientation. In that case, the excited spin waves at similar wavelengths appear at higher frequencies compared to the vortex state without any magnetic bias field applied as shown in Fig. 6 for a 50 nm CoFeB film [samples CoFeB50a (elliptical disk 7.5 μm vs 5 μm axes) and CoFeB50b (circular disk of 3 μm diameter) for measurements without and with a field, respectively] (see also SM movie M6). For the highest wavevector of the experimentally observed spin waves of $\sim$9.5 rad/μm, there is a change in frequency from 16.1 to 25.1 GHz. The calculations indicate that this is the case for both the fundamental and first higher-order mode. From the calculated dispersion curves, it can additionally be seen that their slopes become less steep in the case of an applied magnetic bias field. This coincides with a shift in the ferromagnetic resonance ($k = 0$) from $\sim$1 to 19 GHz. To the right-hand side of the dispersion, exemplary TR-STXM snapshots of the quasi-uniform mode for the cases with and without the magnetic field applied are shown.

IV. SUMMARY AND OUTLOOK

We demonstrated that TR-STXM is able to image spin-wave dynamics at frequencies up to 30 GHz and with wavelengths down to 70 nm by exploiting a low-alpha optics synchrotron operation mode, providing an increased time resolution compared to standard operation. TR-STXM in low-alpha mode thus enables measurements of spin waves at a combined temporal and spatial resolution (order or magnitude: 10 ps and 10 nm) that is at present inaccessible by any other measurement technique. Using low-alpha TR-STXM, several spin-wave modes were imaged in patterned disks with spin vortex ground state for both coupled ferromagnetic bilayers with antiparallel alignment and single-layer ferromagnetic elements. For the coupled ferromagnetic bilayers, it was shown that the collective acoustic modes for local antiparallel magnetization orientation are identical, regardless of the vortex circulation states of the disk element. The frequency range, as compared to previous measurements, was extended, and non-reciprocal acoustic modes of both the short- and long-wavelength branch, as well as an instance of an optical mode, were imaged. For the case of single ferromagnetic layers in the Damon–Eshbach geometry, several propagating spin-wave modes were measured. These dynamics were attributed to both the commonly known quasi-uniform Damon–Eshbach mode but also to modes of higher thickness order (perpendicular standing spin waves) through a comparison with the results from micromagnetic calculations. Due to the extended observable frequency range, spin waves at frequencies up to 30 GHz were observed, presumably belonging to the fourth-order thickness mode. Furthermore, it was shown how the dispersion relations in single-layer systems can be tuned by changing material properties, film thicknesses, and magnetic fields. For both sample systems, it was confirmed that the predictions from micromagnetic theory are valid even at this so far unexplored combination of time- and length scales.

Our results demonstrate that TR-STXM could be used for the imaging of high-frequency spin dynamics in highly anisotropic ferromagnets, ferrimagnetic, and even some antiferromagnetic systems. A further improvement of the time resolution in x-ray imaging could be realized via future synchrotron technology (upgrades such as BESSY variable pulse length storage ring (VSR) or newly build storage rings), time-of-arrival detection schemes,[82] free electron lasers, or laboratory-based higher-harmonics sources. At the same time, complementary advances in spin-dynamic imaging can be expected from TR scanning probe microscopies, near-field magneto-optic Kerr effect (MOKE) microscopy, and TR TEM.

SUPPLEMENTARY MATERIAL

See the supplementary material that consists of a text file ("Supplementary Materials") and 6 animated display items (movies) ("M1–M6"). The text file contains a description of the details of all movies and Supplementary Fig. S1, the latter displaying additional spin-wave line profiles with respect to Fig. 1.

AUTHOR DECLARATIONS
Conflict of Interest

The authors have no conflicts to disclose.

Author Contributions

S. Mayr: Investigation (equal). **J. Förster:** Investigation (equal). **S. Finizio:** Investigation (equal). **K. Schultheiss:** Investigation (equal). **R. A. Gallardo:** Investigation (equal). **R. Narkowicz:** Investigation (equal). **G. Dieterle:** Investigation (equal). **A. Semisalova:** Investigation (equal). **J. Bailey:** Investigation (equal). **E. Kirk:** Investigation (equal). **A. Suszka:** Investigation (equal). **J. Lindner:** Investigation (equal). **J. Gräfe:** Investigation (equal). **J. Raabe:** Investigation (equal). **G. Schütz:** Investigation (equal). **M. Weigand:** Investigation (equal). **H. Stoll:** Investigation (equal). **S. Wintz:** Conceptualization (equal).

DATA AVAILABILITY

The data that support the findings of this study are available from the corresponding author upon reasonable request.

APPENDIX: ADDITIONAL INFORMATION

1. Sample fabrication

All studied samples were fabricated on 200-nm-thick x-ray transparent Si_3N_4 membranes. The ferromagnetic thin films for the trilayer sample were deposited by electron beam evaporation, whereas the films for the single-layer samples were deposited by

thermal evaporation (NiFe) and dc magnetron sputtering (CoFeB), respectively. For most samples, all lithography steps were performed on the front side of the Si_3N_4 membrane, whereas the film for sample CoFeB50b was deposited on the back side of the membrane. As the sputter deposition rate is lower onto the depth-confined membrane on the back of the chips than onto a flat substrate, this CoFeB film is presumably thinner than the nominal 50 nm.

Except for sample CoFeB50a, the patterning of the disk structures with diameters from 2 to 5 μm was performed by electron beam lithography and lift-off processing. First, a bilayer of the positive resists methyl methacrylate(MMA)/poly(methyl methacrylate) (PMMA) was spincoated onto the membranes. The structures were defined by electron beam lithography, subsequently developed in a methyl isobutyl ketone:isopropyl alcohol (MIBK:IPA) mixture, and then rinsed in IPA. After deposition of the materials, the samples were lifted-off in acetone.

Instead, the elliptical disk of sample CoFeB50a was patterned using negative resist and broad ion beam etching.[27]

On top of the structures, a conductor in the form of a coplanar waveguide (sample CoFeB50b, Si_3N_4 in between) or microstrip (all other samples, directly on top) was patterned via electron beam lithography and lift-off processing. The width of these conductors was 1 μm (CoFeB100, CoFeB50b) and 5 μm (all other samples), respectively. The material for the 200 nm thick Cu conductors was deposited by electron beam evaporation for the trilayer sample and by thermal evaporation for the other samples.

To excite dynamics in the samples, alternating currents are passed through the conductors, which generate alternating magnetic Oersted fields that in our case were on the order of $\mu_0 H = 1$ mT. It is primarily the quasi-uniform in-plane component of these dynamic fields that excites the magnetization dynamics in the disk structures. For samples CoFeB100 and CoFeB50b, however, the disk diameter is larger than the antenna width. Therefore, additional perpendicular dynamic fields are acting on the regions of these samples that are adjacent to the edges of the antenna, whereas sample regions outside of the antenna area are not directly excited in a significant way.

2. Material properties

The following magnetic material parameters were used for the modeling of the spin-wave dispersion relations in the different samples, considering a global g-factor of 2.11. The abbreviations are as follows: thickness (d), saturation magnetization (M_s), exchange constant (A), and uniaxial in-plane anisotropy (K_u). It should be noted that the sets of magnetic parameters provided here represent a particular fit of the problem, while other sets with slightly different parameters may also lead to reasonably good fits of the experimental data.

III.1 Magnetic bilayer (Fig. 4)

$$d^{Co} = 50 \text{ nm}, \quad d^{NiFe} = 50 \text{ nm}, \quad d^{Cu} = 10 \text{ nm}$$
$$M_s^{Co} = 1270 \text{ kA/m}, \quad M_s^{NiFe} = 740 \text{ kA/m}$$
$$A^{Co} = 15 \text{ pJ/m}, \quad A^{NiFe} = 0.85 \text{ pJ/m}$$
$$K_u^{Co} = 1000 \text{ J/m}^3, \quad K_u^{NiFe} = 200 \text{ J/m}^3$$

III.2 Single layers
Multimode spin-wave dynamics (Fig. 5):

$$d^{CoFeB} = 100 \text{ nm}, \quad M_s^{CoFeB} = 1050 \text{ kA/m},$$
$$A^{CoFeB} = 18 \text{ pJ/m}, \quad K_u^{Co} = 200 \text{ J/m}^3$$

Influence of the film thickness (Fig. 6):

$$d^{NiFe} = 30 \text{nm}, \quad M_s^{NiFe} = 800 \text{ kA/m},$$
$$A^{NiFe} = 6 \text{ pJ/m}, \quad K_u^{NiFe} = 200 \text{ J/m}^3$$
$$d^{NiFe} = 50 \text{ nm}, \quad M_s^{NiFe} = 800 \text{ kA/m},$$
$$A^{NiFe} = 6 \text{ pJ/m}, \quad K_u^{NiFe} = 350 \text{ J/m}^3$$
$$d^{NiFe} = 100 \text{ nm}, \quad M_s^{NiFe} = 800 \text{ kA/m},$$
$$A^{NiFe} = 5 \text{ pJ/m}, \quad K_u^{NiFe} = 5 \text{ J/m}^3$$

These NiFe samples were fabricated at different times, which provides a possible explanation for the discrepancies in anisotropy and exchange between different samples. Note that the actual thickness of the nominally 25-nm-thick sample was determined to be 30 nm via the fit.

Influence of magnetic fields (Fig. 6):

$$\text{CoFeB50a} (0 \text{ mT}), \quad d^{CoFeB} = 50 \text{ nm},$$
$$M_s^{CoFeB} = 1100 \text{ kA/m}, \quad A^{CoFeB} = 15 \text{ pJ/m},$$
$$K_u^{Co} = 5 \text{ J/m}^3$$
$$\text{CoFeB50b} (250 \text{ mT}), \quad d^{CoFeB} = 42.5 \text{ nm},$$
$$M_s^{CoFeB} = 1200 \text{ kA/m}, \quad A^{CoFeB} = 15 \text{ pJ/m}, \quad K_u^{Co} = 25 \text{ J/m}^3$$

The reduced thickness of sample CoFeB50b as compared to CoFeB50a presumably originates in the reduced sputter rate onto the depth-confined back of the membrane as explained earlier.

3. Micromagnetic model

We employed the dynamic matrix method to characterize the temporal evolution of the magnetization within a thick ferromagnetic film.[28,83,84] This micromagnetic approach entails partitioning the magnetic medium into small elements,[83,85] followed by generating and diagonalizing a matrix containing information on the energetic terms of the system through the effective fields. For the description of the systems studied in this paper, we have partitioned the films into thin sublayers, where the dynamics of such subsystems are determined through the utilization of the Landau–Lifshitz (LL) equation of motion, represented as follows: $\dot{\mathbf{M}}^{(\nu)} = -\mu_0 \gamma \mathbf{M}^{(\nu)} \times \mathbf{H}^{e(\nu)}$ Here, γ is the gyromagnetic ratio's magnitude, $\mathbf{M}^{(\nu)}$ represents the magnetization of sublayer ν, and $\mathbf{H}^{e(\nu)}$ denotes the effective field acting on the ν-th sublayer.

The magnetization excitations are described assuming small oscillations of magnetization around the equilibrium state, so that we can express the magnetization vector and the effective field as follows: $\mathbf{M}^{(\nu)} = M_{s_\nu} \hat{x} + \mathbf{m}$ and $\mathbf{H}^{e(\nu)} = H_{x_\nu}^{e0} + \mathbf{h}^e$, respectively. Here, $\mathbf{m} = m_{y_\nu} \hat{y} + m_{z_\nu} \hat{z}$ represents the dynamic magnetization, M_{s_ν} is the saturation magnetization of the ν-th sublayer, and $\mathbf{h}^e$ is the dynamic field that is directly proportional to $\mathbf{m}$ in the linearization approach. We have adopted a reference coordinate system (x, y, z), where the z axis aligns with the equilibrium magnetization, the y axis is perpendicular to the magnetic film, and the x axis lies within the film's plane. Thus, assuming that $\mathbf{m} = \mathbf{m}(y) e^{i\omega t}$ with ω denoting the angular frequency, and neglecting second-order terms in $\mathbf{m}(y)$, the Landau–Lifshitz equation of motion can be expressed as

$$i(\omega/\mu_0\gamma)m_{y_\nu}(y) = -m_{z_\nu}(y)H_{x_\nu}^{e0} + M_{s_\nu}h_{z_\nu}^e(y) \quad \text{(A1)}$$

and

$$i(\omega/\mu_0\gamma)m_{z_\nu}(y) = m_{y_\nu}(y)H_{x_\nu}^{e0} - M_{s_\nu}h_{y_\nu}^{e}(y). \qquad (A2)$$

The variation of dynamic magnetization with respect to the y-coordinate results from assuming spin-wave propagation along the y axis, which is perpendicular to the equilibrium magnetization (Damon–Eshbach modes). More precisely, this dependency is described by $\mathbf{m}(y) = \mathbf{m}_k e^{iky}$, where k represents the wave vector. Furthermore, equilibrium considerations implicate that $H_{y_\nu}^{e0} = H_{z_\nu}^{e0} = 0$. Equations (A1) and (A2) can be cast as an eigenvalue problem, expressed as

$$\tilde{\mathbf{A}}\,\mathbf{m}_k = i(\omega/\mu_0\gamma)\mathbf{m}_k. \qquad (A3)$$

Matrix $\tilde{\mathbf{A}}$ contains all the effective field terms associated with the energetic interactions within the system, such as Zeeman, demagnetizing, perpendicular anisotropy, in-plane uniaxial anisotropy, and interlayer terms interconnecting the magnetic sublayers. The interlayer energies arise from the bilinear interlayer exchange, characterized by a strength denoted as J, and the dipolar interaction induced by dynamic magnetic charges on both the surface and within the volume of opposing sublayers. It means that both ferromagnetic exchange coupling between nearest neighbor sublayers and dipolar coupling between all pair combinations of sublayers are considered in the calculations. For the single-layer films, a sublayer thickness between 1 and 4 nm was selected, which is of the order of the exchange length of the considered materials and led to convergent results. Additional information about the calculated interactions and their corresponding matrix elements can be found in Refs. 28 and 84.

To describe the antiparallel magnetic bilayer, a non-magnetic spacing of 10 nm thickness without interlayer exchange is introduced to the calculations and the orientation between the two ferromagnetic layers is set to be antiparallel. Each ferromagnetic layer was discretized into eight sublayers, which led to convergent results.

REFERENCES

[1]F. Bloch, "Zur theorie des ferromagnetismus," Z. Phys. **61**(3–4), 206–219 (1930).

[2]T. Holstein and H. Primakoff, "Field dependence of the intrinsic domain magnetization of a ferromagnet," Phys. Rev. **58**(12), 1098–1113 (1940).

[3]V. V. Kruglyak, S. O. Demokritov, and D. Grundler, "Magnonics," J. Phys. D: Appl. Phys. **43**(26), 260301 (2010).

[4]A. V. Chumak et al., "Magnon spintronics," Nat. Phys. **11**(6), 453–461 (2015).

[5]A. Barman et al., "The 2021 Magnonics roadmap," J. Phys.: Condens. Matter **33**(41), 413001 (2021).

[6]A. V. Chumak et al., "Advances in magnetics roadmap on spin-wave computing," IEEE Trans. Magn. **58**(6), 1 (2022).

[7]L. Landau and E. Lifshits, "On the theory of the dispersion of magnetic permeability in ferromagnetic bodies," Phys. Z. Sowjetunion **8**, 153 (1935).

[8]F. Schulz et al., "Realization of a magnonic analog adder with frequency-division multiplexing," AIP Adv. **13**(1), 015115 (2023).

[9]L. Körber et al., "Pattern recognition in reciprocal space with a magnon-scattering reservoir," Nat. Commun. **14**(1), 3954 (2023).

[10]A. Papp, W. Porod, and G. Csaba, "Nanoscale neural network using non-linear spin-wave interference," Nat. Commun. **12**(1), 6422 (2021).

[11]Z. Z. Zhang et al., "Magnon scattering modulated by omnidirectional hopfion motion in antiferromagnets for meta-learning," Sci. Adv. **9**(6), eade7439 (2023).

[12]D. Lachance-Quirion et al., "Entanglement-based single-shot detection of a single magnon with a superconducting qubit," Science **367**(6476), 425 (2020).

[13]S. O. Demokritov et al., "Bose-Einstein condensation of quasi-equilibrium magnons at room temperature under pumping," Nature **443**(7110), 430–433 (2006).

[14]J. Li, S. Y. Zhu, and G. S. Agarwal, "Magnon-photon-phonon entanglement in cavity magnomechanics," Phys. Rev. Lett. **121**(20), 203601 (2018).

[15]J. S. Pratt, "Qubit entanglement in multimagnon states," Phys. Rev. B **73**(18), 184413 (2006).

[16]H. Y. Yuan et al., "Enhancement of magnon-magnon entanglement inside a cavity," Phys. Rev. B **101**(1), 014419 (2020).

[17]A. G. Gurevich and G. A. Melkov, Magnetization Oscillations and Waves (CRC Press, Boca Raton, 1996).

[18]I. Dzyaloshinsky, "A thermodynamic theory of weak ferromagnetism of antiferromagnetics," J. Phys. Chem. Solids **4**(4), 241–255 (1958).

[19]T. Moriya, "Anisotropic superexchange interaction and weak ferromagnetism," Phys. Rev. **120**(1), 91–98 (1960).

[20]R. W. Damon and J. R. Eshbach, "Magnetostatic modes of a ferromagnet slab," J. Phys. Chem. Solids **19**(3–4), 308–320 (1961).

[21]B. A. Kalinikos and A. N. Slavin, "Theory of dipole-exchange spin-wave spectrum for ferromagnetic-films with mixed exchange boundary-conditions," J. Phys. C **19**(35), 7013–7033 (1986).

[22]C. Kittel, "Excitation of spin waves in a ferromagnet by a uniform RF field," Phys. Rev. **110**(6), 1295–1297 (1958).

[23]M. H. Seavey and P. E. Tannenwald, "Direct observation of spin-wave resonance," Phys. Rev. Lett. **1**(5), 168–169 (1958).

[24]G. Dieterle et al., "Coherent excitation of heterosymmetric spin waves with ultrashort wavelengths," Phys. Rev. Lett. **122**(11), 117202 (2019).

[25]P. Grunberg et al., "Brillouin-scattering of light by spin-waves in thin ferromagnetic-films," J. Appl. Phys. **53**(3), 2078–2083 (1982).

[26]P. Grunberg, "Magnetostatic spin-wave modes of a heterogeneous ferromagnetic double-layer," J. Appl. Phys. **52**(11), 6824–6829 (1981).

[27]S. Wintz et al., "Magnetic vortex cores as tunable spin-wave emitters," Nat. Nanotechnol. **11**(11), 948–953 (2016).

[28]V. Sluka et al., "Emission and propagation of 1D and 2D spin waves with nanoscale wavelengths in anisotropic spin textures," Nat. Nanotechnol. **14**(4), 328 (2019).

[29]Z. Zhang et al., "Using ferromagnetic-resonance as a sensitive method to study temperature-dependence of interlayer exchange coupling," Phys. Rev. Lett. **73**(2), 336–339 (1994).

[30]J. Y. Zhou et al., "Ultrafast laser induced precessional dynamics in antiferromagnetically coupled ferromagnetic thin films," Phys. Rev. B **101**(21), 214434 (2020).

[31]D. D. Stancil, Theory of Magnetostatic Waves (Springer, Berlin, 1993).

[32]V. S. L'vov, Wave Turbulence under Parametric Excitation (Springer, Berlin, 1994).

[33]M. Madami et al., "Direct observation of a propagating spin wave induced by spin-transfer torque," Nat. Nanotechnol. **6**(10), 635–638 (2011).

[34]V. E. Demidov et al., "Spin-orbit-torque magnonics," J. Appl. Phys. **127**(17), 170901 (2020).

[35]E. Schlomann, "Generation of spin waves in nonuniform magnetic fields. I. Conversion of electromagnetic power into spin-wave power + vice versa," J. Appl. Phys. **35**(1), 159 (1964).

[36]Y. Au et al., "Resonant microwave-to-spin-wave transducer," Appl. Phys. Lett. **100**(18), 182404 (2012).

[37]H. M. Yu et al., "Omnidirectional spin-wave nanograting coupler," Nat. Commun. **4**, 2702 (2013).

[38]H. M. Yu et al., "Approaching soft X-ray wavelengths in nanomagnet-based microwave technology," Nat. Commun. **7**, 11255 (2016).

[39]S. J. Hermsdoerfer et al., "A spin-wave frequency doubler by domain wall oscillation," Appl. Phys. Lett. **94**(22), 223510 (2009).

[40]N. J. Whitehead et al., "Theory of linear spin wave emission from a Bloch domain wall," Phys. Rev. B **96**(6), 064415 (2017).

[41]R. B. Hollander et al., "Magnetic domain walls as broadband spin wave and elastic magnetisation wave emitters," Sci. Rep. **8**, 13871 (2018).

[42]B. Van de Wiele et al., "Tunable short-wavelength spin wave excitation from pinned magnetic domain walls," Sci. Rep. **6**, 21330 (2016).

[43]C. Behncke et al., "Spin-wave interference in magnetic vortex stacks," Commun. Phys. **1**, 50 (2018).

[44]L. J. Chang et al., "Spin wave injection and propagation in a magnetic nano-channel from a vortex core," Nano Lett. **20**(5), 3140–3146 (2020).

[45]S. Mayr et al., "Spin-wave emission from vortex cores under static magnetic bias fields," Nano Lett. **21**(4), 1584–1590 (2021).

[46]D. O. Ruiz *et al.*, "Unidirectional emission and reconfigurability of channeled spin waves from a vortex core in a teardrop-shaped nanopatch," Phys. Rev. B **104**(9), 094427 (2021).

[47]J. L. Chen, J. F. Hu, and H. M. Yu, "Chiral emission of exchange spin waves by magnetic skyrmions," ACS Nano **15**(3), 4372–4379 (2021).

[48]T. Wessels *et al.*, "Continuous illumination picosecond imaging using a delay line detector in a transmission electron microscope," Ultramicroscopy **233**, 113392 (2022).

[49]N. R. da Silva *et al.*, "Nanoscale mapping of ultrafast magnetization dynamics with femtosecond Lorentz microscopy," Phys. Rev. X **8**(3), 031052 (2018).

[50]B. Pigeau *et al.*, "Measurement of the dynamical dipolar coupling in a pair of magnetic nanodisks using a ferromagnetic resonance force microscope," Phys. Rev. Lett. **109**(24), 247602 (2012).

[51]K. Liang *et al.*, "Ultrafast dynamics revealed with time-resolved scanning tunneling microscopy: A review," ACS Appl. Opt. Mater. **1**, 924 (2023).

[52]T. J. Silva and S. Schultz, "A scanning near-field optical microscope for the imaging of magnetic domains in reflection," Rev. Sci. Instrum. **67**(3), 715–725 (1996).

[53]P. S. Keatley *et al.*, "A platform for time-resolved scanning Kerr microscopy in the near-field," Rev. Sci. Instrum. **88**(12), 123708 (2017).

[54]M. F. Collins *et al.*, "Critical and spin-wave scattering of neutrons from iron," Phys. Rev. **179**(2), 417 (1969).

[55]N. B. Brookes *et al.*, "Spin waves in metallic iron and nickel measured by soft x-ray resonant inelastic scattering," Phys. Rev. B **102**(6), 064412 (2020).

[56]R. Vollmer *et al.*, "Spin-wave excitation observed by spin-polarized electron energy loss spectroscopy: A new method for the investigation of surface- and thin-film spin waves on the atomic scale," Thin Solid Films **464**, 42–47 (2004).

[57]K. Zakeri *et al.*, "Direct probing of the exchange interaction at buried interfaces," Nat. Nanotechnol. **8**(11), 853–858 (2013).

[58]J. R. Sandercock and W. Wettling, "Light-scattering from thermal acoustic magnons in yttrium iron-garnet," Solid State Commun. **13**(10), 1729–1732 (1973).

[59]O. Wojewoda *et al.*, "Observing high-k magnons with Mie-resonance-enhanced Brillouin light scattering," Commun. Phys. **6**(1), 94 (2023).

[60]J. Jersch *et al.*, "Mapping of localized spin-wave excitations by near-field Brillouin light scattering," Appl. Phys. Lett. **97**(15), 152502 (2010).

[61]T. Sebastian *et al.*, "Micro-focused Brillouin light scattering: Imaging spin waves at the nanoscale," Front. Phys. **3**, 35 (2015).

[62]W. Schilz, "Spin-wave propagation in epitaxial Yig films," Philips Res. Rep. **28**(1), 50–65 (1973).

[63]M. Bailleul *et al.*, "Spin waves propagation and confinement in conducting films at the micrometer scale," Europhys. Lett. **56**(5), 741–747 (2001).

[64]H. Stoll *et al.*, "High-resolution imaging of fast magnetization dynamics in magnetic nanostructures," Appl. Phys. Lett. **84**(17), 3328–3330 (2004).

[65]S. B. Choe *et al.*, "Vortex core-driven magnetization dynamics," Science **304**(5669), 420–422 (2004).

[66]B. Van Waeyenberge *et al.*, "Magnetic vortex core reversal by excitation with short bursts of an alternating field," Nature **444**(7118), 461–464 (2006).

[67]M. Weigand *et al.*, "TimeMaxyne: A shot-noise limited, time-resolved pump-and-probe acquisition system capable of 50 GHz frequencies for synchrotron-based X-ray microscopy," Crystals **12**(8), 1029 (2022).

[68]A. Jankowiak and G. Wüstefeld, "Low-α operation of BESSY II and future plans for an Alternating Bunch Length Scheme BESSY VSR," Synchrotron Radiat. News **26**, 22–24 (2013).

[69]N. Träger *et al.*, "Direct imaging of high-frequency multimode spin wave propagation in cobalt-iron waveguides using x-ray microscopy beyond 10 GHz," Phys. Status Solidi RRL **14**(12), 2000373 (2020).

[70]Y. Acremann *et al.*, "Software defined photon counting system for time resolved x-ray experiments," Rev. Sci. Instrum. **78**(1), 014702 (2007).

[71]A. Puzic *et al.*, "Photon counting system for time-resolved experiments in multibunch mode," Synchrotron Radiat. News **23**, 26–32 (2010).

[72]C. Cheng and W. E. Bailey, "Sub-micron mapping of GHz magnetic susceptibility using scanning transmission x-ray microscopy," Appl. Phys. Lett. **101**(18), 182407 (2012).

[73]H. Stoll *et al.*, "Imaging spin dynamics on the nanoscale using x-ray microscopy," Front. Phys. **3**, 26 (2015).

[74]S. Bonetti *et al.*, "Microwave soft x-ray microscopy for nanoscale magnetization dynamics in the 5–10 GHz frequency range," Rev. Sci. Instrum. **86**(9), 093703 (2015).

[75]G. Schütz *et al.*, "Absorption of circularly polarized x-rays in iron," Phys. Rev. Lett. **58**(7), 737–740 (1987).

[76]S. Wintz *et al.*, "Interlayer-coupled spin vortex pairs and their response to external magnetic fields," Phys. Rev. B **85**(22), 224420 (2012).

[77]L. Neel, "Magnetisme - Sur un nouveau mode de couplage entre les animantations de deux couches minces ferromagnetiques," C. R. Hebd. Seances Acad. Sci. **255**(15), 1676 (1962).

[78]S. S. Cherepov *et al.*, "Core-core dynamics in spin vortex pairs," Phys. Rev. Lett. **109**(9), 097204 (2012).

[79]R. A. Gallardo *et al.*, "Reconfigurable spin-wave nonreciprocity induced by bipolar interaction in a coupled ferromagnetic bilayer," Phys. Rev. Appl. **12**(3), 034012 (2019).

[80]E. Albisetti *et al.*, "Optically inspired nanomagnonics with nonreciprocal spin waves in synthetic antiferromagnets," Adv. Mater. **32**(9), 1906439 (2020).

[81]L. Giovannini *et al.*, "Spin excitations of nanometric cylindrical dots in vortex and saturated magnetic states," Phys. Rev. B **70**(17), 172404 (2004).

[82]S. Finizio, S. Mayr, and J. Raabe, "Time-of-arrival detection for time-resolved scanning transmission x-ray microscopy imaging," J. Synchrotron Radiat. **27**, 1320–1325 (2020).

[83]Y. Henry, O. Gladii, and M. Bailleul, "Propagating spin-wave normal modes: A dynamic matrix approach using plane-wave demagnetizing tensors," arXiv:1611.06153 (2016).

[84]R. A. Gallardo *et al.*, "Spin-wave non-reciprocity in magnetization-graded ferromagnetic films," New J. Phys. **21**, 033026 (2019).

[85]L. Körber *et al.*, "Finite-element dynamic-matrix approach for propagating spin waves: Extension to mono- and multi-layers of arbitrary spacing and thickness," AIP Adv. **12**(11), 115206 (2022).

27 February 2025 10:12:26